

<sup>1</sup> Millikelvin precise temperature monitoring system for the  
<sup>2</sup> ProtoDUNE-SP liquid argon detector at CERN

<sup>3</sup> M. Antonova<sup>a</sup>, J. Capó<sup>a</sup>, A. Cervera<sup>a</sup>, P. Fernández<sup>a</sup>, M. Á. García-Peris<sup>a,1,\*</sup>, X. Pons<sup>b</sup>

<sup>a</sup>*Instituto de Fisica Corpuscular Catedratico Jose Beltran 2 E-46980 Paterna (Valencia) Spain*

<sup>b</sup>*CERN Espl. des Particules 1 1211 Meyrin Switzerland*

---

<sup>4</sup> **Abstract**

The precise monitoring of temperatures —to the level of a few milli-Kelvin— is crucial for the operation of large-scale cryostats. In particular, the performance of Liquid Argon Time Projection Chambers —such as those planned for DUNE— heavily relies on proper argon purification and mixing, which can be characterized by a sufficiently dense grid of high-precision temperature probes. In this article, a novel technique for the cross-calibration of Resistance Temperature Detectors (RTDs) in cryogenic liquids (argon and nitrogen) is presented, obtaining an unprecedented precision of 2.5 mK.

<sup>5</sup> *Keywords:* Detectors, Liquid Argon, Cryogenics, Temperature, RTD, Purity,

<sup>6</sup> Computational Fluid Dynamics

---

<sup>7</sup> **1. Introduction**

<sup>8</sup> The Deep Underground Neutrino Experiment (DUNE) [2], expected to be taking  
<sup>9</sup> data towards the end of the decade, aims at performing comprehensive neutrino oscillation analyses, —broadly exploring the Charge-Parity violation parameters phase-space  
<sup>10</sup> and resolving the neutrino-mass hierarchy problem [6]. Its vast physics program also  
<sup>11</sup> includes searches for hypothetical proton decay channels [3], multi-messenger astronomy  
<sup>12</sup> from supernovae and neutrino bursts [8], and explorations of Beyond the Standard  
<sup>13</sup> Model (BSM) physics [7]. With the most powerful neutrino beam ever built, produced at  
<sup>14</sup> Fermilab, the experiment follows the long-baseline neutrino oscillations approach, with  
<sup>15</sup>

---

\*Corresponding author

Email address: [miguel.garcia-peris@manchester.ac.uk](mailto:miguel.garcia-peris@manchester.ac.uk) (M. Á. García-Peris)

<sup>1</sup> now in the University of Manchester

16 two detectors. The Near Detector, also at Fermilab, will characterize the unoscillated  
17 neutrino beam. The Far Detector (FD), located in the Sandford Underground Research  
18 Facility (SURF), 1300 away from the ND and 1.5 km underground, will measure the  
19 oscillated flux.

20 DUNE phase I far detector will have two Liquid Argon Time Projection Chambers  
21 (LArTPC) and DUNE phase II will complement with two more modules with an expected  
22 fiducial mass of 40k tons. The detector technology has been established, with excellent  
23 tracking and calorimetric capabilities, in several smaller-scale experiments [10, 13]. In-  
24 cluded, the first demonstration of the technology at the kilotonne scale, carried out at  
25 the CERN Neutrino Platform as part of the ProtoDUNE program. In particular, the  
26 ProtoDUNE-SP experiment [1] reproduced the detector components of the second DUNE  
27 FD module [4] at a scale 1:1 with a total argon mass 20 times smaller (770 tons). It was  
28 operated from mid-2018 to mid-2020, constituting the largest monolithic LArTPC to be  
29 built and operated up to date [5, 9].

30 Since neutrinos rarely interact, a dense target material is required. The relatively  
31 abundant noble-element argon, which liquified at 87 K has a density of 1.39 g/cm<sup>3</sup>, is ideal  
32 as the active material of a TPC. However, the 3D images produced by charged particles  
33 traversing the detector can be exponentially attenuated by medium impurities such as  
34 mainly nitrogen, oxygen and water. This can introduce bias in energy measurements  
35 by absorbing ionization electrons. In ProtoDUNE-SP, the level of impurities was kept  
36 below 100 ppt oxygen equivalent [1] using a cryogenic recirculation and purification  
37 system. Three purity monitors, based on the ICARUS design [25], were installed outside  
38 the active volume of the TPC to measure the electron lifetime, which is inversely related  
39 to the residual concentration of impurities. They ran twice a day to monitor the argon  
40 purity and thus to provide the necessary corrections for posterior data analysis.

41 Studies based on computational fluid dynamic (CFD) simulations, and the experi-  
42 ence gained with previous LArTPC demonstrators such as LAPD [11] and the 35-tonne  
43 prototype [12, 18], have paved the way to operate large-scale cryostats requiring low con-  
44 centrations of impurities. These studies have also shown that it exists a strong correlation  
45 between temperature and purity in the liquid argon volume. The distribution of impu-  
46 rities is insensitive to small ( $\mathcal{O} \sim 1$  K) absolute temperature variations, but strongly de-

47 pends on the relative vertical temperature gradient. As the bulk volume in the cryostats  
48 needs to be continuously mixed with the incoming purified argon to ensure the purifica-  
49 tion of the whole LAr volume, the temperature distribution acts as a clear indicator of  
50 that mixing: a homogeneous temperature distribution indicates that the liquid is being  
51 properly mixed, whereas large temperature gradients constitute a clear symptom of de-  
52 ficient mixing. If the LAr bulk volume is not mixed properly, a stratification regime can  
53 develop: a significant portion of the liquid remains unpurified, generating ‘dead’ regions  
54 inside the detector. Hence, a constant monitoring of this temperature gradient can iden-  
55 tify and mitigate potential failures of the purification system. In ProtoDUNE-SP, this  
56 gradient was predicted to be about 15 mK by the CFD simulations [1, 4].

57 The CFD simulations also predict, in spite of homogeneous mixing, that the con-  
58 centration of impurities may also vary across the cryostat volume, requiring a position-  
59 dependent electron lifetime correction. The Purity Monitors themselves are intrusive  
60 objects which cannot be deployed inside the active volume, rather in only a few well-  
61 defined locations near the cryostat walls; thus, precise inference of the electron lifetime  
62 map requires alternative methods, as the one proposed in this article. A net of tem-  
63 perature sensors cross-calibrated to the <5 mK level should allow the measurement of  
64 a 15 mK temperature gradient, which can be used to constraint CFD simulations, pro-  
65 viding a data-driven prediction of the impurity concentration. The main limitations of  
66 this new approach are the precision of the cross-calibration of the temperature sensors  
67 and the accuracy of the simulations. In this article, precise temperature monitoring for  
68 ProtoDUNE-SP will be described with particular emphasis on sensor calibration.

## 69 **2. The temperature monitoring system of ProtoDUNE-SP**

70 ProtoDUNE-SP [1] was the single-phase (SP) demonstrator of DUNE far detector  
71 second module [4], currently known as Horizontal Drift (HD) module. The elements  
72 constituting the TPC, its associated readout electronics and the photon detection system,  
73 were housed in a 8x8x8 m<sup>3</sup> cryostat that contains the LAr target material. The cryostat,  
74 a free-standing steel-framed vessel with an insulated double membrane, is based on the  
75 technology used for liquefied natural gas storage and transport. A cryogenic system  
76 maintains the LAr at a stable temperature of about 87 K, and ensures the required purity

77 level by means of a closed-loop process that recovers the evaporated argon, recondenses  
78 it, filters it, and returns it to the cryostat, keeping the LAr level at about 7.3 m from the  
79 bottom membrane. ProtoDUNE-SP was exposed to a charged particle test-beam from  
80 October to November 2018, and later recorded cosmic rays until January 2020 [5, 9]. It  
81 was finally emptied and decommissioned in Summer 2020.

82 In order to understand the LAr behaviour inside the cryostat and validate CFD  
83 simulations, 92 high-precision temperature sensors were installed inside ProtoDUNE-  
84 SP, near the active volume. These sensors were distributed in two vertical arrays, or  
85 Temperature Gradient Monitors (TGM), and two horizontal grids below and above the  
86 TPC, respectively. Three elements were common to all systems: sensors, cables and  
87 readout electronics. RTD technology [22] was chosen for this application. It consists of a  
88 metallic element whose resistance changes with temperature. This resistance is measured  
89 by feeding the RTD with a known current and measuring the resulting voltage. Based  
90 on previous experience from other prototypes [12], Lake Shore PT102 platinum sensors  
91 [21] with 100 ohms resistance at room temperature were chosen. Sensors were mounted  
92 on a 52x14 mm<sup>2</sup> PCB with an IDC-4 connector, such that they could be plugged-in at  
93 any time. Several versions of the PCB have been explored, finally converging to the one  
94 shown in Fig. 1, which minimizes the contact of the sensor with the PCB while keeping  
95 the sensor protected.

96 A careful choice of the readout cable and the proper connections are essential to ob-  
97 tain the required temperature precision. See for example [22] for a detailed description.  
98 A custom cable made by Axon [14] was used. It consists of four American Wire Gauge  
99 (AWG) 28 teflon-jacketed copper wires, forming two twisted pairs, with a metallic ex-  
100 ternal shield and an outer teflon jacket. The outer diameter of the cable is 3.7 mm.  
101 Teflon was chosen for its good thermal properties and low out-gassing. The metallic  
102 external shield (connected to the readout in one end and left floating at the sensor’s end)  
103 and the twisted pairs are crucial to reduce the effect of external electromagnetic noise  
104 pickup. When RTDs are far from the voltmeter, the resistance of cables and connectors  
105 are added to the one of the sensor, biasing the temperature measurement. This bias can  
106 be subtracted to some level, but cannot be fully controlled since the resistance of those  
107 elements also depends on temperature. To minimise the impact of this effect a four wire

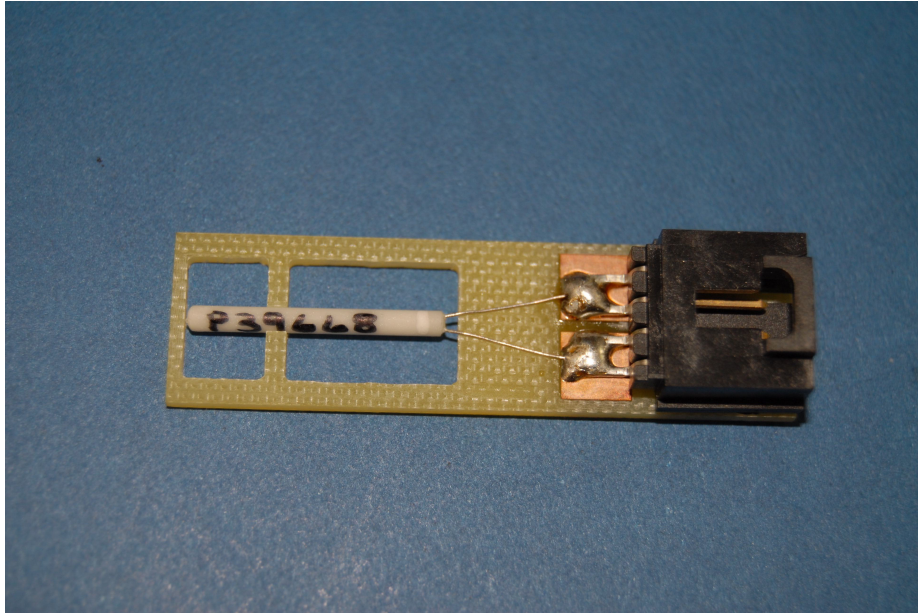


Figure 1: PCB support with temperature sensor and IDC-4 connector. The transition from two wires at the sensor to 4 wires at the readout is clearly seen. The sensor has a length of 2 cm.

108 readout is introduced [22], such that the voltage is measured in the vicinity of the RTD.

109 The last common element is the readout system, consisting of a very precise 1 mA  
110 current source to excite the sensors and a 24 bits ADC to measure the voltage. The  
111 readout system will be described in detail in section 3.

112 As previously mentioned, ProtoDUNE-SP CFD simulations predict vertical temper-  
113 ature gradients as low as 15 mK [1]. A relative precision better than 5 mK was required  
114 to validate and tune those simulations with sufficient confidence. Three main ingredients  
115 are necessary to obtain such a precision: i) high quality and stable temperature probes,  
116 ii) a very precise readout system, and iii) a proper calibration, both for the readout  
117 and the sensors. As mentioned above, two TGMs were deployed in ProtoDUNE-SP: one  
118 could be moved vertically and hence calibrated *in situ*, while the other one —static—  
119 fully relied on a prior calibration in the laboratory. In this article, the calibration of the  
120 static TGM [17] sensors is be described in detail. This device consists of a vertical array  
121 of 48 sensors, installed 20 cm away from the lateral field cage.

122 The calibration was performed once in spring 2018 (a few months before the operation

123 of ProtoDUNE-SP), and several times after ProtoDUNE-SP decommissioning. In this ar-  
124 ticle the calibration setup, procedure and results will be described in detail. Comparison  
125 between the different calibration runs will be addressed, revealing important information  
126 about systematic uncertainties and RTD ageing.

127 **3. Readout system**

128 A precise and stable electronic readout system is needed to achieve the required pre-  
129 cision. In previous versions of the calibration system, each sensor was connected to a  
130 different and independent electronic circuit and thus, fed by a different current and read  
131 by a different ADC channel. It was soon realized that the measured temperature differ-  
132 ence between any two pairs of sensors was heavily affected by the electronic offset between  
133 channels. This offset was not constant, and showed dependence on ambient temperature  
134 and humidity, which affected both the current source and the ADC, generating variations  
135 of tens of mK for the measurement of a single calibration constant between sensors. A  
136 variant of an existing mass PT100 temperature readout system developed at CERN for  
137 one of the LHC experiments [16] was adapted to solve this problem. The system consists  
138 of an electronic circuit that includes:

- 139 • A precise and accurate 1 mA current source for the excitation of the temperature  
140 sensors. Based on an application of the Texas Instruments precise voltage reference  
141 REF102CU with a possibility to adjust  $\pm 10\text{nA}$  with Keithley 2001 multimeter  
142 [15, 23].
- 143 • A multiplexing circuit based on the Analog Devices ADG1407BRUZ multiplexer  
144 with ultralow internal resistance in an 8-channel differential configuration. The  
145 readout circuit contains three multiplexers, providing a readout capacity of 24  
146 channels. The multiplexing circuit and the current sourced are realised in a single  
147 card (see Fig. 2).
- 148 • A readout system based on National Instruments Compact RIO-FPGA device [19]  
149 equipped with a NI-9238 analogue input module that provide 24 bits of resolution  
150 over 1 Volt range [20]. By programming the Van Dusen equation the readout

151 calculates the temperature in Kelvin units. The Compact RIO also drives the  
152 control bits of the multiplexers

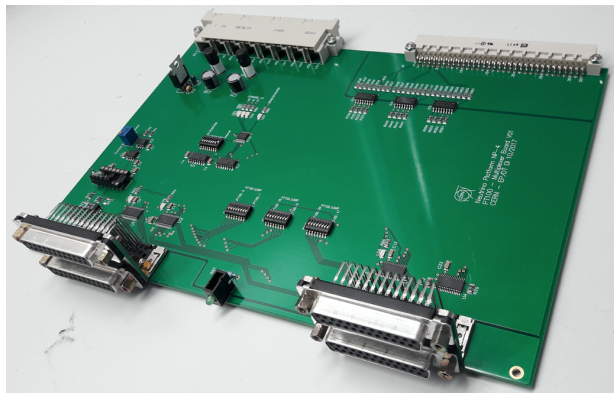


Figure 2: Current source and multiplexing card with 24 channels.

153 One of the features of the readout circuit is the serialization of the current source excita-  
154 tion for all the sensors connected to the same board. The same 1 mA current is delivered  
155 to all sensors connected to the same board. Multiplexing the signal of the sensors such  
156 that they can be readout by the same ADC channel minimises the residual offset due to  
157 the electronics. This system was used during the calibration campaigns presented in this  
158 article and also for the temperature measurements during ProtoDUNE-SP operation.

159 The readout was not considered a potential source of bias during the calibration  
160 campaign prior to the installation in ProtoDUNE-SP (see Sec. 4) and it was not stud-  
161 ied in detail at that time. However, aiming to improve the calibration results after  
162 ProtoDUNE-SP operation, a more thoughtful study of the readout was performed be-  
163 fore the calibration campaigns presented in Sec. 5. In particular, the twelve channels  
164 (7-18) used for sensor calibration were investigated. It was found that, despite the mul-  
165 tiplexing system, a small residual offset between channels still exists. Figure 3 shows  
166 the offsets of channels 8-18 with respect to channel 7, computed using twelve 20 ohms  
167 low Temperature Coefficient of Resistance (TCR)<sup>2</sup> precision resistors, with an equivalent  
168 temperature of 76 K. Two of those, High Precision 1 (HP1) and High Precision 2 (HP2),

---

<sup>2</sup>The temperature coefficient of resistance is defined as the change in resistance per unit resistance per degree rise in temperature. Typically  $\pm 5\text{ppm}/^\circ\text{C}$ .

169 are selected as the measurement samples and connected to the reference channel (7) and  
 170 the channel being calibrated (from 8-18), while leaving all other channels connected to  
 171 other secondary resistors to let the current flow through the system. The readout offset  
 172 between channel 7 and channel X,  $\Delta T_{7-X}^{readout}$ , is then computed using the results of two  
 173 consecutive measurements:

174 1. HP1 in channel 7 and HP2 in the channel X being calibrated. The offset between  
 175 the measured temperatures is

$$\Delta T_{7-X}^A = T_X^{HP2} - T_7^{HP1} + \Delta T_{7-X}^{readout}. \quad (1)$$

176 2. HP2 channel 7 and HP1 in the channel X being calibrated. The offset between the  
 177 measured temperatures is

$$\Delta T_{X-7}^B = T_X^{HP1} - T_7^{HP2} + \Delta T_{7-X}^{readout}. \quad (2)$$

178 Because of the very low TCR of the resistors, it can be assumed that the resistances  
 179 are constants in those two measurements ( $T_7^{HP1} = T_X^{HP1}$  and  $T_7^{HP2} = T_X^{HP2}$ ). Thus,  
 180 the offset between channels 7 and X can be computed as the average between those two  
 181 measurements:

$$\Delta T_{7-X}^{readout} = \frac{\Delta T_{7-X}^A + \Delta T_{X-7}^B}{2}. \quad (3)$$

182 The results in Fig. 3, show an offset of up to 2.5 mK when comparing directly with  
 183 channel 7, while the offset between any other two channels is below 1 mK, indicating  
 184 that there is something special about the first channel being readout. Error bars in that  
 185 figure correspond to the RMS of four independent measurements (repeatability) of the  
 186 same offset (see Fig. 3). As it can be observed the error is below 0.5 mK, what probes  
 187 the great repeatability of the readout. These offsets are more likely due to parasitic  
 188 resistances in the different lines that are multiplexed. This finding allowed a correction  
 189 to the measurements taken during the subsequent calibration campaigns, improving the  
 190 obtained precision.

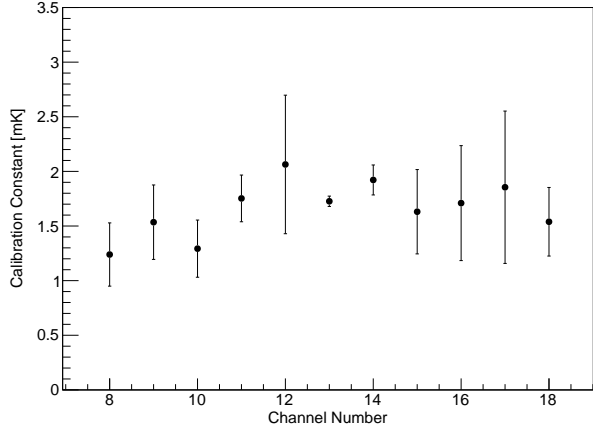


Figure 3: Offset between readout channels 8-18 and channel 7, used as reference. Points correspond to the mean of the 4 independent measurements and the error bars are their RMS.

#### 191 4. Calibration before the installation in ProtoDUNE-SP

192 The Lake Shore Cryotronics company provides PT102 RTDs with a temperature  
 193 reading dispersion of about 0.1 K, which is insufficient for ProtoDUNE-SP's requirements.  
 194 While the company offers additional calibration to the 10 mK level, the cost is prohibitive.  
 195 R&D on sensor calibration was identified as a crucial ingredient for the success of the  
 196 ProtoDUNE-SP temperature monitoring system. For this particular application, sensor  
 197 calibration consists in finding the temperature offsets between any pair of sensors when  
 198 exposing them to the same temperature. The experimental setup used for the calibration  
 199 of RTDs before their installation in ProtoDUNE-SP had two main components: i) the  
 200 readout system used to monitor the sensor's temperature (described in the previous  
 201 section) and ii) the cryogenics vessel and the associated mechanical elements used to put  
 202 sensors together under stable cryogenics conditions. They were developed to achieve a  
 203 relative calibration with a precision better than 5 mK.

##### 204 4.1. Experimental setup

205 The mechanics of the calibration setup evolved considerably since the initial tests until  
 206 the final Static TGM calibration. Offset stability and repeatability drove this evolution.  
 207 The final setup (see Fig. 4) consisted of the following elements:

- A polystyrene vessel formed by an outer box with dimensions  $35 \times 35 \times 30$  cm $^3$  and 4.5 cm thick walls and a dedicated polystyrene cover, complemented by extruded polystyrene panels glued into the inner walls and floor of the outer box, to conform an inner empty volume of  $10 \times 10 \times 20$  cm $^3$ .
- A  $10 \times 10 \times 20$  cm $^3$  3D printed polyactic acid (PLA) box with two independent concentric volumes, placed in the inner volume of the polystyrene vessel. Its purpose is twofold: i) to contain LAr, since polystyrene is porous to it, and ii) to create an smaller inner volume with further insulation and less convection.
- A cylindrical aluminum capsule, to be placed in the inner volume of the PLA box, with 5 cm diameter, 12 cm height and 1 mm thin walls. It had a circular aluminum cover with a small opening to extract the cables and to allow LAr to penetrate inside. The capsule was used to slowly bring sensors to cryogenic temperatures by partial immersion in LAr with no liquid inside, minimizing thermal stress. Aluminum was chosen for its high thermal conductivity.
- A 3D printed PLA support for four sensors, to be placed inside the aluminum capsule, keeping sensors always in the same position with respect to each other and to the capsule walls.

The system described above provides stable conditions in the inner volume, with three levels of insulation: the outer polystyrene vessel and two PLA box LAr volumes. The aluminium capsule is key to this system and its usage constituted a turning point in the R&D since it minimises thermal shocks, which were identified as the main limiting factor for the repeatability of the sensor's offsets. Indeed, variations of several tenths of mK were observed in initial tests without the capsule. The problem was attributed to thermal shocks when, after many immersions in LN<sub>2</sub>, one of the sensors suffered a dramatic change in its offset (see Fig 5-top). Examination at the microscope revealed cracks in the outer RTD ceramics (see Fig 5-bottom).

#### *4.2. Calibration procedure*

The calibration procedure relies on the assumption that all sensors in the capsule are at the same temperature. This limits the number of RTDs in a single run to four, since i)



Figure 4: Final calibration setup. Left: polystyrene box with PLA box and aluminum capsule. Middle: aluminum capsule. Right: Sensor's support with four sensors.

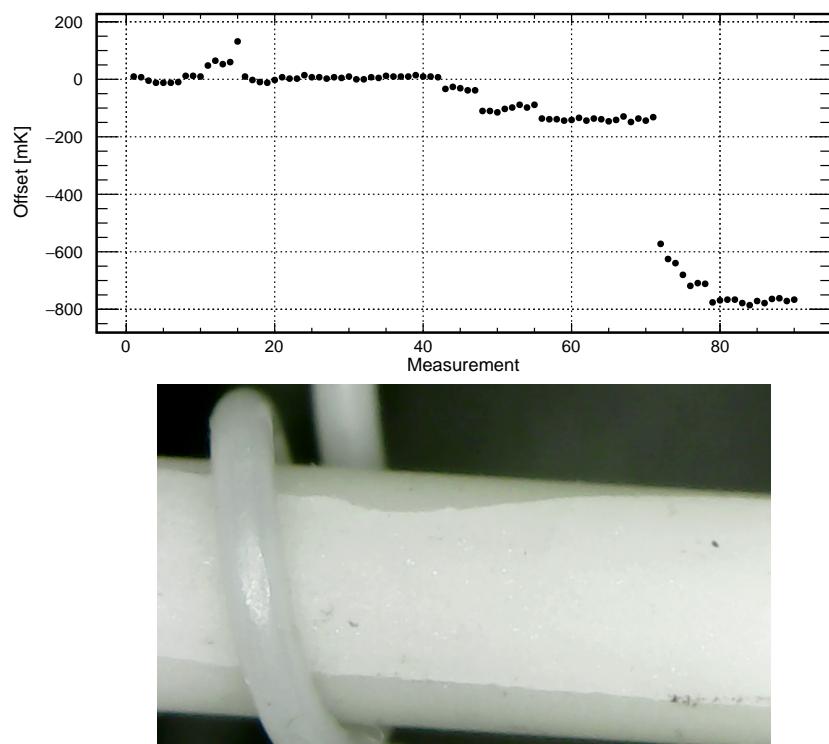


Figure 5: Top: offset between two sensors for 90 immersions in LN<sub>2</sub>. A drop of 800 mK is observed. Bottom: cracks observed with the microscope in the ceramic of the sensor.

237 they should be as close as possible to each other and ii) as far as possible to the capsule  
 238 walls (the sensor closer to the wall could be biased). Two different methods, described  
 239 schematically in Fig. 6, were used to cross-calibrate all 48 sensors in runs of 4 sensors:

- 240 1. **Reference method:** all sensors are calibrated with respect to a reference one, in  
 241 sets of three sensors (the fourth one would be the reference sensor, which must be  
 242 present in all runs). In total there are sixteen calibration sets.
- 243 2. **Tree method:** Four different sets of sensors can be cross-calibrated by performing  
 244 a second round of measurements with a single promoted sensor from each of those  
 245 four sets. Since there are 16 sets in total, a third round of measurement is needed  
 246 to cross-calibrate the four sets in the second round.

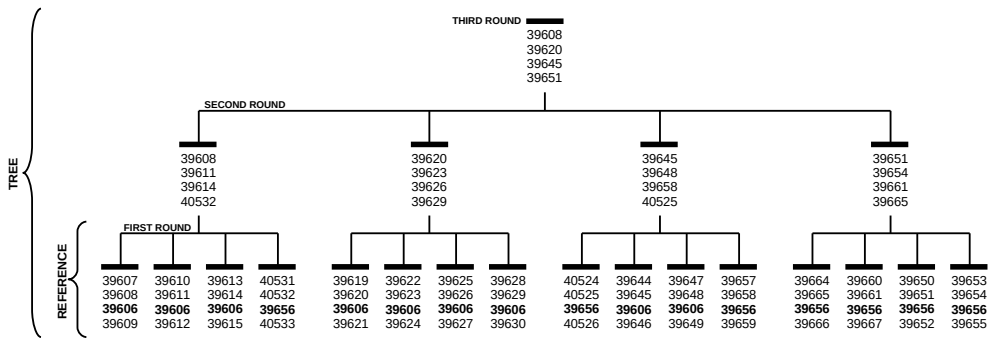


Figure 6: Schematic view of calibration sequence. Each number represents a different RTD, and the numbers in bold represent the reference sensors. The first round consists on a direct calibration respect to a reference sensor. The second and third rounds are needed to relate all sensors independently of the reference sensor.

247 The reference method was expected to be more precise since any two sensors were  
 248 related through a single intermediate sensor (the reference one), while for the tree method  
 249 the relation between any two sensors required more than one intermediate sensor. For  
 250 example, the offset between sensors  $i$  and  $j$  in different sets, related through sensors  $k$   
 251 and  $l$  in the second round, would be  $\Delta T_{ij} = \Delta T_{ik} + \Delta T_{kl} + \Delta T_{lj}$ . For sensors related  
 252 through the third round an additional term should be added, further increasing the offset  
 253 error.

254 Offset repeatability is one of the key parameters to be understood since the laboratory  
 255 calibration must be applicable to the real detector. This was studied by performing four

256 independent calibration runs for each set of four sensors. However, because thermal  
257 fatigue of the reference sensor (64 thermal cycles for 4 repeatability runs) was a strong  
258 concern, three secondary reference sensors were used to regularly monitor the response  
259 of the primary reference sensor.

260 The following procedure is applied for each set of four sensors. First, they are placed  
261 inside the aluminium capsule. The sensor with the highest serial number is placed in the  
262 orange connector, and the one with the lowest in the red. The central connector closer to  
263 the red one is used for the reference sensor. These positions are easily called by numbers  
264 from 1 (orange) to 4 (red), as shown in Fig. 7.

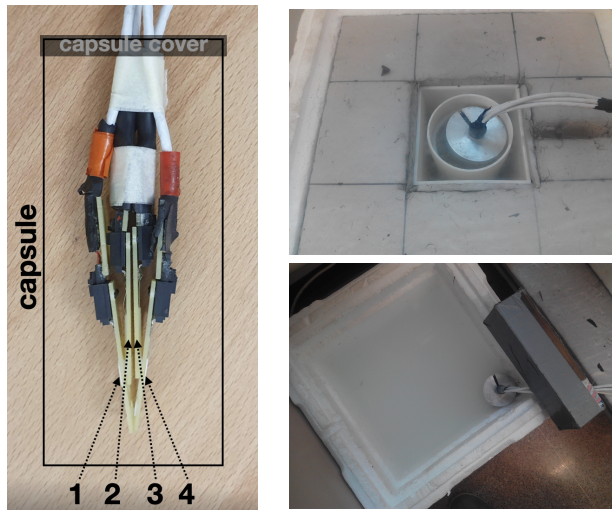


Figure 7: Left: Picture of sensor order inside the flask. Position 1 corresponds to highest serial number and 4 to lowest; position 3 is reserved to reference sensor. Middle: Flask partially introduced in LAr. Right: Flask partially introduced in room water to warm up sensors before performing a new measurement.

265 After filling the PLA box with LAr, the aluminum capsule is partially immersed  
266 (see Fig. 7-middle) such that the air inside cools-down slowly, avoiding direct exposure  
267 of the sensors to LAr, which would result in a thermal shock. When the monitored  
268 temperature approaches the one of LAr (< 95 K), which takes about 15 minutes, the  
269 capsule is completely immersed, being filled with liquid. The PLA box is then completely  
270 filled with LAr to account for evaporation during the cool-down phase. Finally, the  
271 polystyrene vessel is closed using the polystyrene lid. The actual calibration runs for  
272 forty minutes.

273 When the measurement is finished, the capsule is extracted from the liquid, emptied  
 274 of LAr and partially immersed into another polystyrene box filled with water at room  
 275 temperature (see Fig. 7-right). The warm-up process takes about ten minutes. When  
 276 sensors have reached a temperature around 250 K a new independent measurement can  
 277 start.

278 Figure 8 shows the typical evolution of the temperature for the four sensors in the  
 279 capsule during the warm-up and cool-down processes. A sudden fall to 87 K is observed at  
 280 about 1950 seconds, which corresponds to total immersion of the sensors in LAr. Notice  
 281 also that two of the sensors have lower temperature during the cool-down process; those  
 282 are sensors 1 and 4, the ones closer to the capsule walls.

283 For each set of sensors the procedure described above is repeated four times, resulting  
 284 in four independent measurements of the same offset. These measurements are used to  
 285 compute a mean offset value and its standard deviation (repeatability from now on).

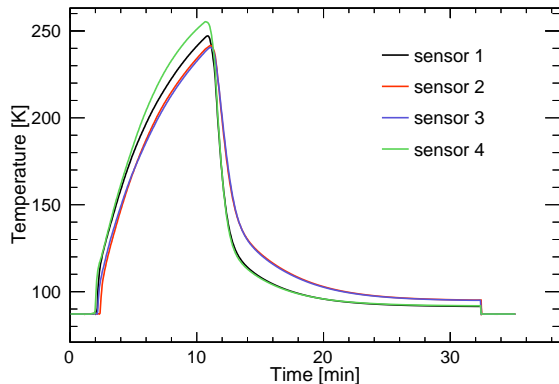


Figure 8: Temperature evolution during the warm-up and cool-down processes between two consecutive runs.

#### 286 4.3. Calibration results

287 Here we present the results of the calibration using both calibration methods, a  
 288 study of the consistency of these results, and a preliminary estimation of the systematic  
 289 uncertainty of the calibration process.

290    4.3.1. Results on the first round of measurements

291    Fig. 9 shows the offset of three different sensors with respect to the reference sensor  
 292    as a function of time, and for four independent calibration runs. The offset is more  
 293    stable for the sensor closer to the reference (position 2), while external sensors (positions  
 294    1 and 4) have larger variations, but present similar patterns between them. This effect  
 295    is attributed to the geometry of the system, with sensors at different heights and not  
 296    symmetrically positioned with respect to the capsule walls, and was taken into account  
 297    when developing the second version of the system, presented in Sec. 5.

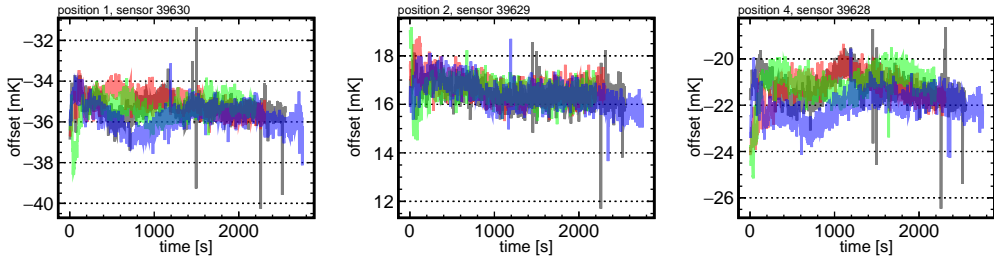


Figure 9: Offset between the reference sensor and each of the three sensors in a set, as a function of time. Each colour represents an independent measurement.

298    The mean offset for each sensor and each calibration run is computed as the average  
 299    in the time range between 1000 and 2000 seconds, found to be the most stable region for  
 300    most sensors. The standard deviation of the four measurements is taken as the statistical  
 301    error of the offset, also referred from now on as repeatability. As shown in Fig. 10, those  
 302    errors are in general below 1 mK, demonstrating the great level of repeatability achieved.

303    4.3.2. Time walk correction for reference sensors

304    Time evolution of the response of sensor 39606 was studied by periodically (every  
 305     $\sim$ 20 immersions) computing its offset with respect to three secondary reference sensors,  
 306    39603, 39604 and 39605. For each of those additional calibrations, two runs were taken  
 307    instead of four in order to minimize thermal fatigue of the reference sensor. As shown  
 308    in Fig. 11-left, the offset, computed as the mean of those two runs, varies linearly at a  
 309    rate of 0.07 mK/immersion, which suddenly increases to 0.22 mK/immersion after 60  
 310    runs. This change in the slope may be related with the frequency of immersions, which  
 311    increased from 3/day to 5/day. Sensor 39606 was initially used for other purposes, and  
 312    the calibration of the 48 sensors conforming the static TGM started approximately at

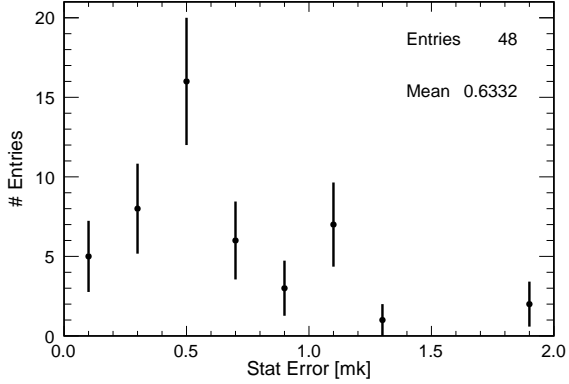


Figure 10: Distribution of the offset statistical error for calibration runs in the first round.

313 immersion 40. Given this change in its response, sensor 39606 was substituted by 39656  
 314 as primary reference for the last quarter of the TGM calibration in order to avoid further  
 315 fatigue and potential untraceable behaviour. The evolution of the new reference sensor  
 316 is shown in Fig. 11-right. It is worth noting that the same slopes are valid for the three  
 317 secondary reference sensors in both cases, supporting the idea that the change observed  
 318 in the offsets can be exclusively attributed to thermal fatigue of the reference sensor.

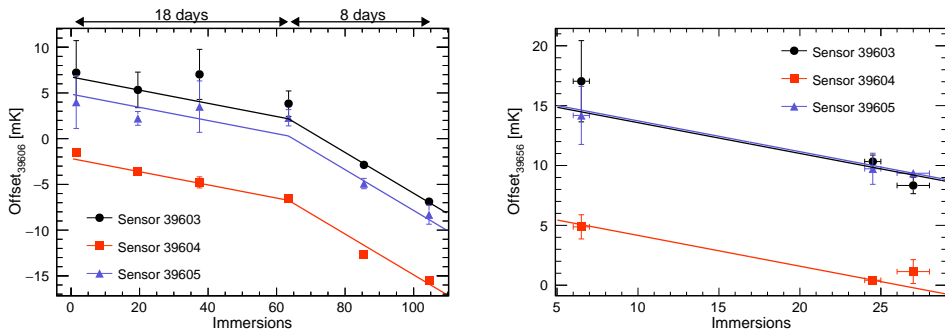


Figure 11: Offset between the reference sensor 39606 and the three secondary references as a function of the number of immersions. Offsets for sensor 39604 have smaller errors because of its position inside the capsule. Solid lines are correspond to the parameterisation in Eq. 4.

319 The zero intercept in both panels of Fig. 11 corresponds to the unbiased offset (or the  
 320 offset at  $N_{\text{immersions}} = 0$ ) of each of the secondary reference sensors with respect to the  
 321 primary reference. In order to compute the unbiased offset for a sensor  $s$ , a time walk  
 322 correction after  $N$  immersions is calculated as

$$\Delta T_{s,06}(N = 0) = \begin{cases} \Delta T_{s,06}(N) + (0.072 \pm 0.003) * N & N < 63.5 \\ \Delta T_{s,06}(N) + (0.072 \pm 0.003) * 63.5 + \\ +(0.223 \pm 0.007) * (N - 63.5) & N > 63.5, \end{cases} \quad (4)$$

$$\Delta T_{s,56}(N = 0) = \Delta T_{s,56}(N) + (0.168 \pm 0.007) * N. \quad (5)$$

323 All sensors can be related to the same primary reference sensor, 39606, adding the  
 324 unbiased offset between sensors 39606 and 39656,  $\Delta T_{56,06}(N = 0)$ , to sensors calibrated  
 325 with respect to 39656. By averaging over the three secondary reference sensors, the value  
 326 obtained is  $\Delta T_{56,06}(N = 0) = -9.19 \pm 0.13$  mK.

327 *4.3.3. Results on the reference method*

328 Fig. 12-top shows the offset of all sensors with respect to the 39606 reference. As it can  
 329 be noticed, the dispersion of the offsets is compatible with the  $\sim 0.1$  K dispersion quoted  
 330 by the vendor. Fig. 13-left shows the distribution of the repeatability of the computed  
 331 calibration constants after applying the different corrections, showing an average value  
 332 below 1 mK.

333 *4.3.4. Results on the tree method*

334 The offsets are computed in this case with respect to an arbitrary reference among  
 335 all sensors being calibrated. Selecting as reference a sensor present in the third round  
 336 (see Fig. 6) minimises the number of operations to compute the offset, and hence the  
 337 statistical error. Fig. 12-bottom shows the offset of each sensor with respect to sensor  
 338 39645, chosen as reference. Fig. 13-right shows the distribution of the repeatability of  
 339 the computed calibration constants, the mean of which is slightly below the one obtained  
 340 for the reference method. Thus, it is confirmed that despite the higher number of inter-  
 341 mediate sensors to relate any two sensors, the additional error introduced by the time  
 342 walk correction makes the tree method superior to the reference method. Moreover, the  
 343 reference method suffers a —not yet known— systematic error associated to the time  
 344 wall correction model.

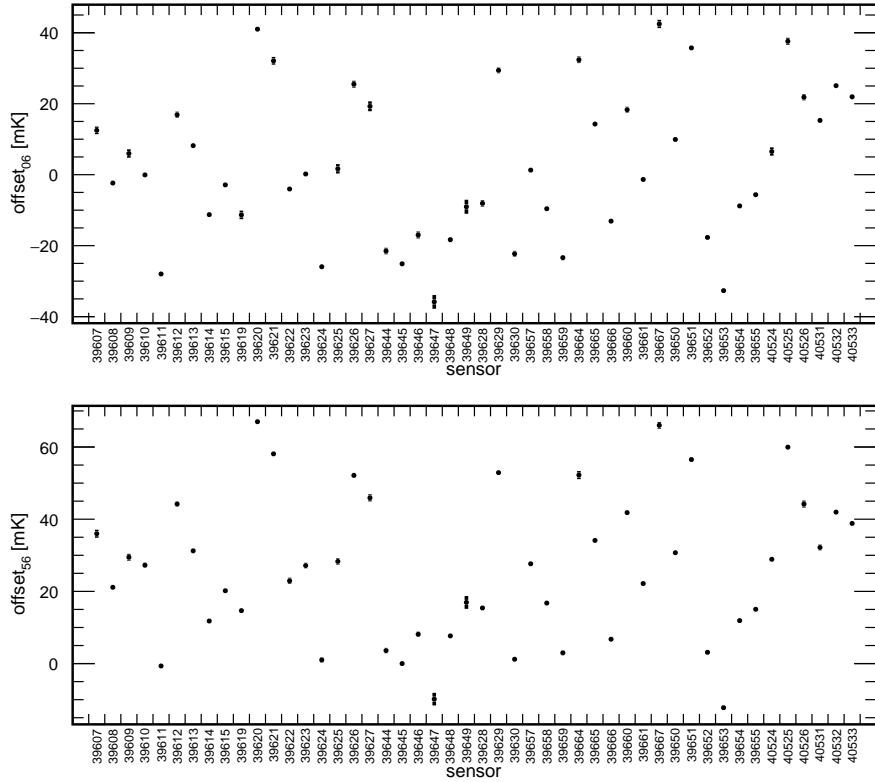


Figure 12: Top: offset distribution with respect to reference sensor 39606 using the reference method. Bottom: offset distribution with respect to reference sensor 39656 using the tree method.

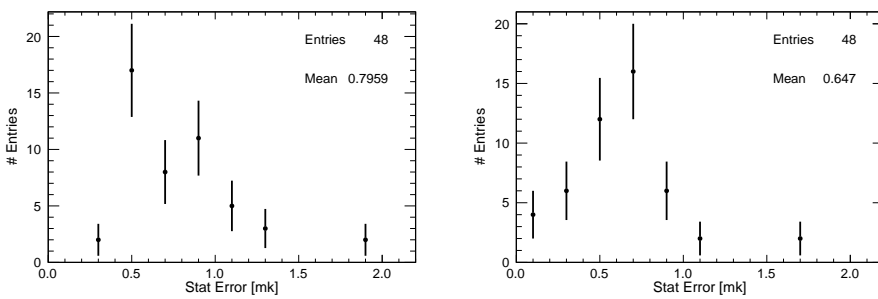


Figure 13: Left: repeatability distribution for reference method. Right: repeatability distribution for tree method.

345    4.3.5. *Consistency cross-check and error estimation*

346    The errors presented so far are in general below 1 mK, and they correspond to the  
347    standard deviation of the four independent measurements of each calibration constant  
348    plus the error propagation associated to the required corrections (time-walk for the refer-  
349    ence method, addition of calibration constants for the tree method, and the uncorrected  
350    electronic residual offset for both). These corrections are likely to include unknown sys-  
351    tematic effects in the final calibration constants. In order to estimate the overall final  
352    precision of the calibration, the following cross-check was performed. The calibration  
353    strategy provides two different calibration constants for each sensor, one for the refer-  
354    ence method and another for the tree method. In the case of the sixteen sensors used in  
355    the second round of the calibration tree, these two values are statistically independent  
356    of each other, since they rely on different runs. Indeed, the reference method uses only  
357    the runs in the first round while the tree method for those sensors uses only runs in the  
358    second and third round. Thus, those 16 sensors can be used to estimate the precision of  
359    the calibration procedure by comparing the results of the two methods.

360    By construction, the result of subtracting the calibration constants obtained in the  
361    two methods should be compatible with the offset between sensors 39645 and 39606,  
362     $\Delta T_{45,06} = \Delta T_{s,06} - \Delta T_{s,45} = T_{45} - T_{06}$ , used as reference for the tree and reference  
363    methods respectively. This offset is found to be  $-25.1 \pm 0.7$  mK by direct measurement  
364    of the two sensors (see 10th column in Fig. 6). Fig. 14 shows this benchmark with (left)  
365    and without (right) time walk corrections for the 16 sensors aforementioned, probing  
366    the self-consistency of this correction. The standard deviation of this distribution, 2.4  
367    mK, is an estimation of the quadratic sum of the total uncertainty of both calibrations.  
368    Assuming that the reference sensor method has a larger uncertainty than the tree method  
369    due to the time walk correction, we can set a superior limit for the total error of the  
370    three method of 1.7 mK. In the same way, this is the inferior limit for the total error of  
371    the reference method. In both cases, these errors are less than half of what was originally  
372    required for the TMS.

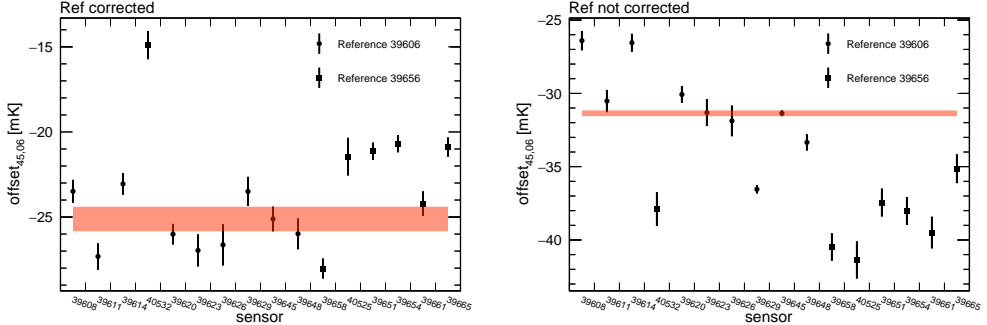


Figure 14:  $\Delta T_{45,06}$  computed through all sensors of the second stage of the calibration procedure. Left: applying corrections. Right: not applying corrections. A clear improvement is obtained using the corrections on the reference sensor. The red line represents the expected value of this calibration constant.

### 373 5. Re-calibration after ProtoDUNE-SP operation

374 After ProtoDUNE-SP decommissioning in 2020, temperature sensors were discon-  
 375 nected from the TGM and re-calibrated several times (see Table 1), using both LAr and  
 376 LN2 as cryogenic liquid. The comparative analysis of those re-calibrations not only offers  
 377 insights into the long-term stability of the sensors but also elucidates any potential de-  
 378 pendencies on the choice of the cryogenic liquid. Although DUNE will use LAr, massive  
 379 RTD calibration would benefit from using LN2, given its higher accessibility and lower  
 380 cost in Spain.

date	cryogenic liquid	# sensors in capsule
March 2018	LAr	4
February 2022	LN2	14
March 2023	LN2	14
July 2023	LAr	14

Table 1: Calibration runs with indication of the date, the cryogenic liquid used and the number of sensors inside the capsule.

381 In this section, a description of the setup used for these new calibrations, the changes  
 382 applied to the procedure as well as the results and conclusions of these calibrations are  
 383 presented.

384    *5.1. Evolution of the calibration setup*

385    The Horizontal Drift far detector module will have more than 500 precision sensors  
386 [4], making the use of the calibration setup impractical for calibration purposes, since it  
387 can only accommodate four sensors simultaneously. Significant modifications have been  
388 introduced in order to increase this number to twelve, while maintaining the calibration  
389 precision achieved during the 2018 calibration campaign. This was accomplished by posi-  
390 tioning sensors at the same height, to avoid any potential vertical gradient, and following  
391 a cylindrical configuration, under the assumption that convection inside the capsule has  
392 cylindrical symmetry. This symmetry is also kept outside the capsule in all concentric  
393 cryogenic containers, having added a fourth independent cryogenic volume which should  
394 further reduce convection inside the inner capsule. This notable advancement greatly  
395 streamlines the calibration process and serves to reduce both statistical and systematic  
396 errors associated with the procedure. Fig. 15 shows the different elements of the new  
397 calibration setup, which are described below:

- 398    • A polystyrene box with dimensions  $55 \times 35 \times 30 \text{ cm}^3$  and 4.5 cm thick walls with  
399 a dedicated cover of the same material.
- 400    • Extruded polystyrene rectangles with a cylindrical hole of 12.5 cm diameter and  
401 25 cm height, to conform the inner volume.
- 402    • A PTFE container with 12.5 cm diameter, 25 cm height and 2 mm thick walls to  
403 fit in the hole left in the box. The approximate volume is 2 L.
- 404    • A 3D printed PLA cylinder with two independent concentric volumes, placed inside  
405 the PTFE container.
- 406    • A cylindrical aluminum capsule to be placed in the inner volume of the PLA cylin-  
407 der. It has 7 cm diameter, 14 cm height and 1 mm thick walls.
- 408    • A 3D printed PLA holder for 14 sensors, 12 of them forming a circle (the ‘corona’)  
409 and 2 of them in the center, to be used as references. This support can be attached  
410 to the aluminum capsule at a fixed height. Cables are naturally extracted from the  
411 top of the assembly. A detailed view of this holder can be found in Fig. 15.

- 412     • The readout electronics, described in Sec. 3 have been retained from the previous  
 413     setup.
- 414     • A more cost effective cable with similar performance has been used. Produced by  
 415     TempSens [24], it has four twisted cables instead of two separated twisted pairs  
 416     and an additional Kapton insulation layer between the shielding mesh and the four  
 417     conductors. Its diameter is 2.7 mm.

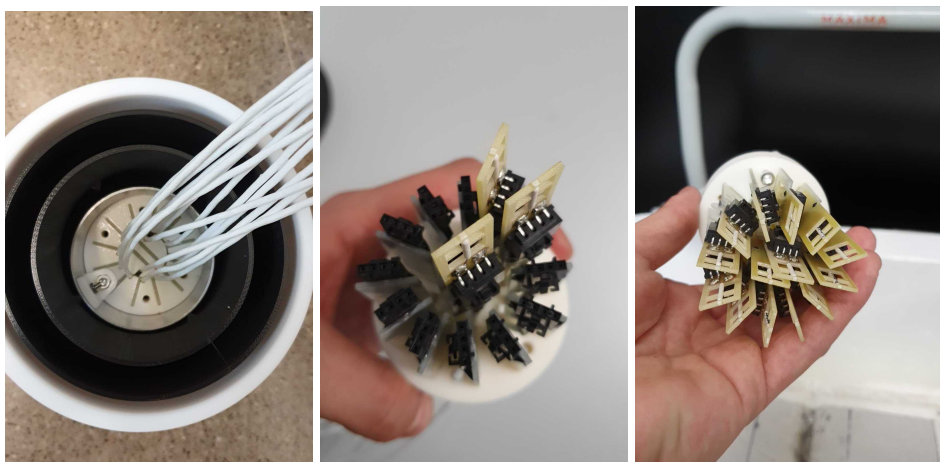


Figure 15: Left: The four concentric volumes. Center: A view of one of the references and two corona sensors. Right: The 12 corona sensors plus the 2 references.

418     *5.2. Calibration procedure*

419     The sensor support was originally designed to accommodate two reference sensors  
 420     in the center (see Fig. 15), enabling both the reference and tree calibration methods.  
 421     However, it was soon observed that temperature variations between corona and reference  
 422     sensors were significantly larger than those between any two corona sensors. This effect  
 423     was attributed to the convection happening inside the capsule, which favour sensors dis-  
 424     tributed symmetrically with respect to the geometry of the system. This can be observed  
 425     in Fig. 16-left, where the offset between two corona sensors is nearly constant in time  
 426     in four independent measurements, and in Fig. 16-right, where the offset between a  
 427     corona and a reference sensor shows a more chaotic behaviour. Consequently, only the  
 428     ‘tree’ calibration method was considered during the calibrations after ProtoDUNE-SP  
 429     decommissioning.

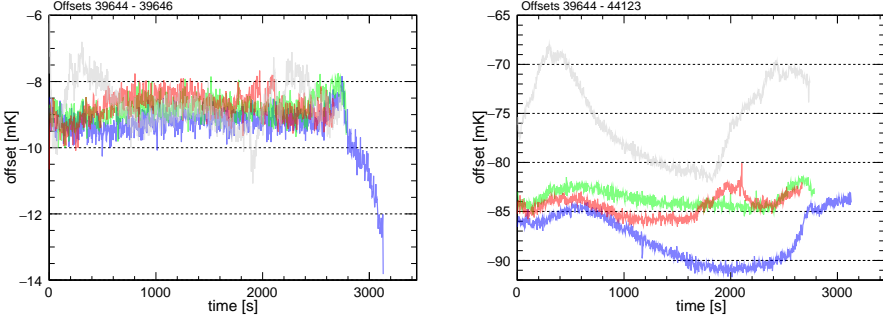


Figure 16: Left: The 4 measured offsets between two arbitrary sensors in the corona. Right: The 4 measured offsets between a sensor in the corona and one of the references, at the center.

430        The new calibration tree, shown in Fig. 17, contemplates four 12-sensors sets in the  
 431        first round, and a unique second round with three promoted sensors from each of the  
 432        sets in the first round. With this scheme, promoted sensors only suffer 8 baths, avoiding  
 433        the necessity of a time-walk correction.

434        The experimental procedure is similar to the one presented in Sec. 4, with two small  
 435        differences. First, the several concentric vessels are cooled down for 40 minutes before  
 436        introducing the aluminum capsule for the first time in a day, slightly improving the  
 437        results of the first calibration run. Second, the warm up process is accelerated using a  
 438        heat gun, avoiding the use of water.

439        *5.3. Calibration results*

440        Due to the fact that three sensors per set are raised to form the second-round set,  
 441        exist several combinations of those raised sensors in order to compute a certain offset  
 442        between a given pair of sensors. Each of these combinations is called a path on the  
 443        calibration tree, or simply a *path*. There are  $3^2$  paths that serve to compute the offset  
 444        between a given pair of sensors, at first order. One can arbitrarily chose any sensor  
 445        as absolute reference to compute all the other offsets with respect to this one. If one  
 446        wisely choose the absolute reference to be a sensor that has been raised in any of the 4  
 447        first-round sets, the number of independent paths for a given pair of sensors reduces to  
 448        only 3. The chosen absolute reference is the 40525 for the rest of this analysis.

449        For each of the paths, the error on the offset can be computed by quadratically adding  
 450        the individual errors on each of the terms contributing to that specific offset. Then, the

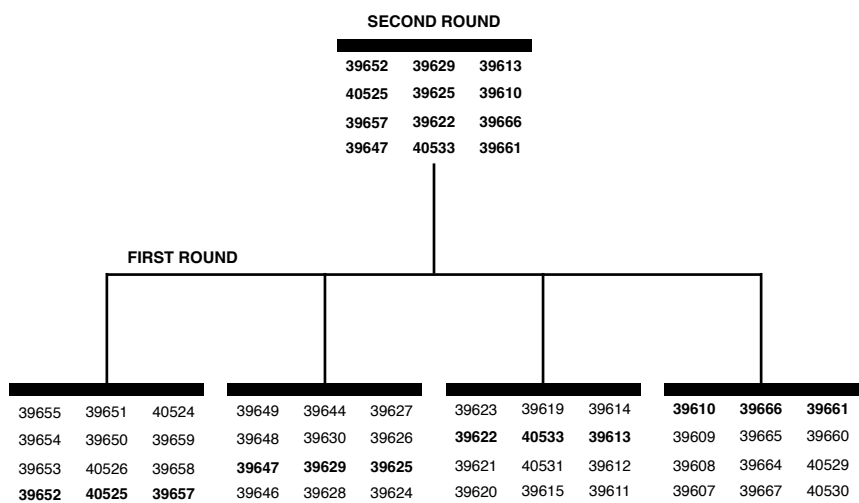


Figure 17: Schematic of the calibration strategy used with the new setup. Each of the sets contains 12 sensors, all of them placed in the corona, plus 2 references at the center. Sensors in bold in the first round are promoted to the second.

451 average path offset is computed as the weighted mean of the different paths by considering  
 452 the different path offsets errors that are involved. Finally, the error on the average path  
 453 offset is computed as the standard deviation of the involved path offsets.

454 Fig. 18 shows the distribution of the repeatability (defined in Sec. 4.3.1) for the  
 455 three new calibrations mentioned in Table 1. In all three cases the error is slightly  
 456 above 1 mK. As expected, this error is larger than in the 2018 calibration mainly due  
 457 to the increased size of the inner volume and the larger distance between sensors. This  
 458 hypothesis is supported by Fig. 19, showing the statistical error as a function of the  
 459 distance to the reference sensor in the corona for a particular measurement. However,  
 460 there is no substantial difference between the repeatability obtained for LN2 and LAr  
 461 calibrations.

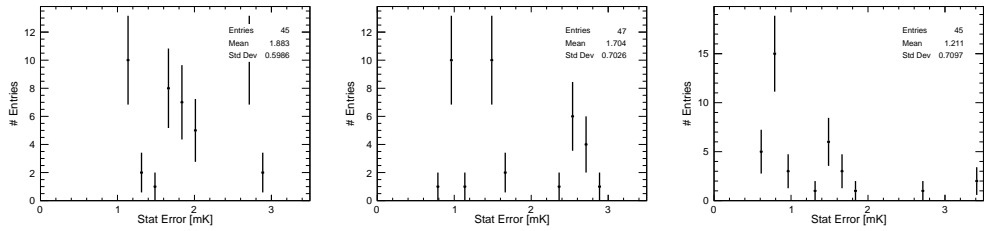


Figure 18: Statistical error distribution for the new calibrations. Left: LN2-2022. Middle: LN2-2023, Right:LAr-2023

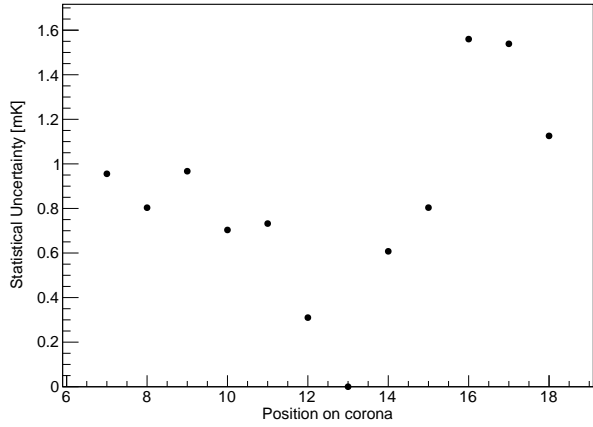


Figure 19: Statistical error vs position in corona for the first run of the first calibration set, using position 13 as reference.

462 Comparison between LN2 and LAr calibrations can also be used to understand the  
 463 dependence of the calibration constants on the absolute temperature. Fig. 20 shows the  
 464 difference between the calibration constants obtained in two calibrations. The RMS of  
 465 the distribution is lower when comparing two calibrations in the same liquid (LN2 in this  
 466 case). However no bias is observed when comparing calibrations in two different liquids,  
 467 indicating that offsets are insensitive to a 10 K variation in absolute temperature.

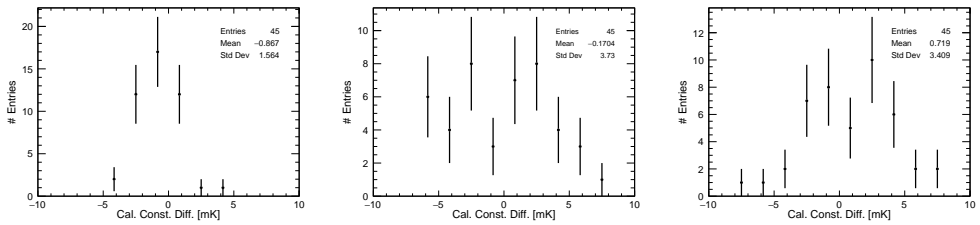


Figure 20: Difference between offsets for two calibrations. Left: LN2-2023 and LN2-2022. Middle: LAr-2023 and LN2-2022. Right: LAr-2023 and LN2-2023.

468 Ageing and long term stability have also been addressed. The left panel of Fig. 20  
 469 shows no difference between the offsets calculated in LN2 with a delay of one year. A bet-  
 470 ter understanding of this effect is achieved by comparing with the LAr-2018 calibration,  
 471 as shown in the next section.

#### 472 5.4. Comparison between new and old calibrations

473 Fig. 21 shows the distribution of the offset difference between the LAr-2018 and  
 474 LAr-2023 calibrations. The mean of the distribution is  $0.8 \pm 0.6$  mK, excluding any  
 475 relevant systematic drift. The RMS of the distribution, 3.9 mK, is only slightly larger  
 476 than the ones obtained in the comparison between newer calibrations, which could be  
 477 due to the unknown contribution of the uncorrected readout offsets, pointing to small  
 478 or non-existing ageing effects. This can also be observed in Table 2, summarizing the  
 479 results of all possible comparisons between calibration campaigns, showing the mean and  
 480 RMS of those comparisons. The lowest RMS, 2.6 mK, is obtained for the LN2-2022 to  
 481 LN2-2023 combination, which is somehow expected since i) the cryogenic liquid is the  
 482 same, ii) ageing should be small since there is only one year difference and iii) having  
 483 use the same readout channels, readout offsets cancel out.

484 The difference between the constants obtained in two calibration campaigns can

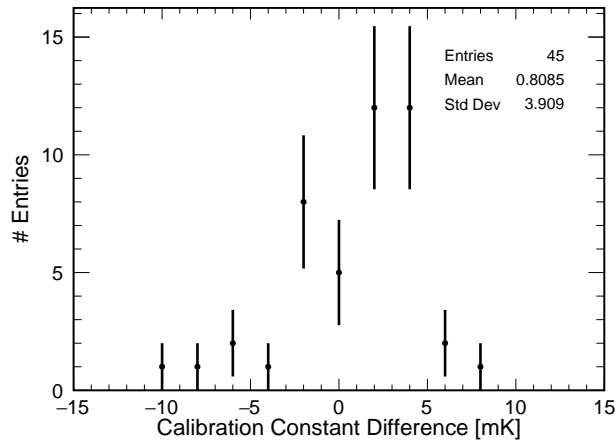


Figure 21: Difference between offsets for LAr-2018 and LAr-2023 calibrations.

	LAr-2018	LN2-2022	LN2-2023	LAr-2023
LAr-2018	-	-0.7, 3.6	0.3, 4.7	0.3, 3.9
LN2-2022	-	-	1.0, 2.6	0.5, 3.4
LN2-2023	-	-	-	-0.5, 3.7
LAr-2023	-	-	-	-

Table 2: Mean and RMS of the difference between the calibration constants obtained in two calibration campaigns.

485 be used to estimate the total calibration error. Since ProtoDUNE Horizontal Drift  
486 (ProtoDUNE-HD), the next iteration of the ProtoDUNE-SP detector, and DUNE will  
487 use LAr, the best estimation of the error would come from a LAr to LAr comparison  
488 close in time to the actual detector running. Being this combination not available, three  
489 other combinations can be used. The combination LN2-2022 LN2-2023 has a RMS of  
490 2.6 mK, which should be the quadratic sum of the the errors of individual calibrations.  
491 Assuming this error is the same for both campaigns the single calibration error would  
492 be 1.8 mK. In this comparison the readout channel offsets cancel out, but real fluctua-  
493 tions in those offsets contribute to the estimated single calibration error. Comparison  
494 between LAr-2018 and LAr-2023 also brings some insights into the single calibration  
495 error. The RMS is in this case 3.9 mK, corresponding to a single calibration error of 2.8  
496 mK. However, this value includes the uncorrected readout offsets as well as the effect  
497 of some potential ageing. Finally, comparison between LAr and LN2 calibrations in the  
498 new campaigns, avoids the readout offset and ageing problems, but suffer from potential  
499 dependence on the cryogenic liquid. Those comparisons have similar RMS of the order  
500 of 3.5 mK, corresponding to a single calibration error of 2.5 mK. This figure establishes  
501 an upper limit on the LAr calibration error. One can safely conclude that the individual  
502 calibration error in LAr is in the range 1.8-2.5 mK. This value is consistent with the one  
503 obtained using a different method for the LAr-2018 calibration, 2.4 mK (see Sec. 4.3.5).

## 504 6. Conclusions

505 The DUNE experiment will require the construction and operation of the largest  
506 cryostats ever used in a particle physics experiment. This makes the continuous mea-  
507 surement of temperature gradients in liquid argon crucial for monitoring the stability  
508 of the cryogenics system and for detector calibration. R&D on the calibration of RTD  
509 probes started in 2017, leading to promising results for sensors installed in the DUNE  
510 prototype at CERN.

511 The first setup proved the viability of the method, obtaining a calibration error of 2.4  
512 mK. A key component was the readout electronics, with an intrinsic resolution better  
513 than 0.5 mK in the comparison between two channels. The mechanics was also crucial,  
514 with several insulation layers consisting of independent concentric volumes, ensuring

515 minimal convection in the inner volume. Sensors were contained in an aluminium capsule,  
516 enabling slow cool-down and warm-up processes, found to be fundamental to guarantee  
517 the integrity of the sensors and to minimize the effect of ageing.

518 The calibration system was later enhanced to accommodate the large-scale calibration  
519 required for the DUNE detectors. The capacity of the inner capsule was increased from  
520 4 to 14 sensors, while improvements were made to the insulation and symmetry of the  
521 system to minimize temperature differences between sensors. The new system has slightly  
522 worst repeatability for sensors in the same set, but reduces the statistical and systematic  
523 errors associated to the calibration tree, needed to relate any two sensors in different  
524 calibration sets. Calibration with the new setup has achieved a precision in the range of  
525 1.8-2.5 mK, substantially better than the 5 mK DUNE requirement.

526 Another difference between the new and old calibrations is the use of a different  
527 cryogenic liquid. While DUNE will use LAr, LN<sub>2</sub> is cheaper and more accessible in  
528 Spain, simplifying the process of massive calibration for DUNE detectors. The 10 K  
529 difference between those liquids has a minimal effect on the calibration constants.

530 A comparison of the four calibration campaigns has provided valuable insights into  
531 aging effects, with no evidence of RTD aging observed over a five-year period. This  
532 highlights the stability and reliability of the PT-102-based system.

## 533 7. Acknowledgments

534 The present research has been supported and partially funded by Conselleria d'Innovació,  
535 Universitats, Ciència i Societat Digital, by the Fundació 'La Caixa', and by MICINN.  
536 The authors would also like to thank all the people involved in the installation,  
537 commissioning and operation of ProtoDUNE-SP, specially to Stephen Ponders. Finally,  
538 the authors would also like to thank Nicholas Lane for his writing suggestions.

## 539 References

- 540 [1] Abi, B., et al. (DUNE), 2017. The Single-Phase ProtoDUNE Technical Design Report  
541 [arXiv:1706.07081](https://arxiv.org/abs/1706.07081).
- 542 [2] Abi, B., et al. (DUNE), 2020a. Deep Underground Neutrino Experiment (DUNE), Far Detector  
543 Technical Design Report, Volume I Introduction to DUNE. JINST 15, T08008. doi:10.1088/  
544 1748-0221/15/08/T08008, [arXiv:2002.02967](https://arxiv.org/abs/2002.02967).
- 545 [3] Abi, B., et al. (DUNE), 2020b. Deep Underground Neutrino Experiment (DUNE), Far Detector  
546 Technical Design Report, Volume II: DUNE Physics [arXiv:2002.03005](https://arxiv.org/abs/2002.03005).

- 547 [4] Abi, B., et al. (DUNE), 2020c. Deep Underground Neutrino Experiment (DUNE), Far Detector  
 548 Technical Design Report, Volume IV: Far Detector Single-phase Technology. JINST 15, T08010.  
 549 doi:10.1088/1748-0221/15/08/T08010, arXiv:2002.03010.
- 550 [5] Abi, B., et al. (DUNE), 2020d. First results on ProtoDUNE-SP liquid argon time projection  
 551 chamber performance from a beam test at the CERN Neutrino Platform. JINST 15, P12004.  
 552 doi:10.1088/1748-0221/15/12/P12004, arXiv:2007.06722.
- 553 [6] Abi, B., et al. (DUNE), 2020e. Long-baseline neutrino oscillation physics potential of the DUNE  
 554 experiment. Eur. Phys. J. C 80, 978. doi:10.1140/epjc/s10052-020-08456-z, arXiv:2006.16043.
- 555 [7] Abi, B., et al. (DUNE), 2021a. Prospects for beyond the Standard Model physics searches  
 556 at the Deep Underground Neutrino Experiment. Eur. Phys. J. C 81, 322. doi:10.1140/epjc/  
 557 s10052-021-09007-w, arXiv:2008.12769.
- 558 [8] Abi, B., et al. (DUNE), 2021b. Supernova neutrino burst detection with the Deep Under-  
 559 ground Neutrino Experiment. Eur. Phys. J. C 81, 423. doi:10.1140/epjc/s10052-021-09166-w,  
 560 arXiv:2008.06647.
- 561 [9] Abud, A.A., et al. (DUNE), 2022. Design, construction and operation of the ProtoDUNE-SP Liquid  
 562 Argon TPC. JINST 17, P01005. doi:10.1088/1748-0221/17/01/P01005, arXiv:2108.01902.
- 563 [10] Acciarri, R., et al. (MicroBooNE), 2017. Design and Construction of the MicroBooNE Detector.  
 564 JINST 12, P02017. doi:10.1088/1748-0221/12/02/P02017, arXiv:1612.05824.
- 565 [11] Adamowski, M., et al., 2014. The Liquid Argon Purity Demonstrator. JINST 9, P07005. doi:10.  
 566 1088/1748-0221/9/07/P07005, arXiv:1403.7236.
- 567 [12] Adams, D.L., et al., 2020. Design and performance of a 35-ton liquid argon time projection chamber  
 568 as a prototype for future very large detectors. JINST 15, P03035. doi:10.1088/1748-0221/15/03/  
 569 P03035, arXiv:1912.08739.
- 570 [13] Amerio, S., et al. (ICARUS), 2004. Design, construction and tests of the ICARUS T600 detector.  
 571 Nucl. Instrum. Meth. A 527, 329–410. doi:10.1016/j.nima.2004.02.044.
- 572 [14] Axon, . Axon custom cables. URL: [https://www.axon-cable.com/en/00\\_home/00\\_start/00/index.aspx](https://www.axon-cable.com/en/00_home/00_start/00/index.aspx). last visited: 2022-10-01.
- 573 [15] application bulletin, B.B., . Implementation and applications of current sources and current re-  
 574 ceivers. URL: <https://www.ti.com/lit/an/sboa046/sboa046.pdf?ts=1712062207089>. last visited:  
 575 2024-04-02.
- 576 [16] Chojnacki, E., 2009. A Multiplexed RTD Temperature Map System for Multi-Cell SRF Cavities,  
 577 in: SRF2009, p. 232.
- 578 [17] García-Peris, M.A., 2018. ProtoDUNE T-Gradient development and calibration. Master's thesis.  
 579 Valencia U. doi:10.2172/1780813.
- 580 [18] Hahn, A., Adamowski, M., Montanari, D., Norris, B., Reichenbacher, J., Rucinski, R., Stewart,  
 581 J., Tope, T. (LBNE), 2016. The LBNE 35 Ton Prototype Cryostat, in: 2014 IEEE Nuclear Sci-  
 582 ence Symposium and Medical Imaging Conference and 21st Symposium on Room-Temperature  
 583 Semiconductor X-ray and Gamma-ray Detectors. doi:10.1109/NSSMIC.2014.7431158.
- 584 [19] Instruments, N., a. Compactrio systems. URL: <https://www.ni.com/es/shop/compactrio.html>. last  
 585 visited: 2024-04-02.
- 586 [20] Instruments, N., b. Ni-9238. URL: <https://www.ni.com/es-es/shop/model/ni-9238.html>. last  
 587 visited: 2024-04-02.
- 588 [21] LakeShore, . Platinum sensors applications. URL: <https://www.lakeshore.com/products/categories/overview/temperature-products/cryogenic-temperature-sensors/platinum>. last  
 589 visited: 2023-05-18.
- 590 [22] Minco, . Resistance thermometry. URL: <https://www.minco.com/wp-content/uploads/Resistance-Thermometry.pdf>. last visited: 2023-05-18.
- 591 [23] Tektronix, . Keithley 2001 digit high performance multimeter. URL: [https://download.tek.com/datasheet/1KW-73954-1\\_2001-2002\\_DMM\\_Datasheet\\_080323.pdf](https://download.tek.com/datasheet/1KW-73954-1_2001-2002_DMM_Datasheet_080323.pdf). last visited: 2024-04-02.
- 592 [24] TempSens, . Rtd cables. URL: <https://tempsens.com/catalog/cables-wires/rtd-triad-cables.html>. last visited: 2024-03-15.
- 593 [25] Xiao, Y. (DUNE), 2021. Purity monitoring for ProtoDUNE-SP. J. Phys. Conf. Ser. 2156, 012211.  
 594 doi:10.1088/1742-6596/2156/1/012211.